



HAL
open science

Dual-band LSPR of tungsten bronze nanocrystals tunable over NIR and SWIR ranges

Yannis Cheref, Florian Lochon, Louise Daugas, Capucine Cleret de Langavant, Éric Larquet, Alexandre Baron, Thierry Gacoin, Jongwook Kim

► **To cite this version:**

Yannis Cheref, Florian Lochon, Louise Daugas, Capucine Cleret de Langavant, Éric Larquet, et al.. Dual-band LSPR of tungsten bronze nanocrystals tunable over NIR and SWIR ranges. *Chemistry of Materials*, In press, 10.1021/acs.chemmater.2c02879 . hal-03834806

HAL Id: hal-03834806

<https://hal.science/hal-03834806>

Submitted on 31 Oct 2022

HAL is a multi-disciplinary open access archive for the deposit and dissemination of scientific research documents, whether they are published or not. The documents may come from teaching and research institutions in France or abroad, or from public or private research centers.

L'archive ouverte pluridisciplinaire **HAL**, est destinée au dépôt et à la diffusion de documents scientifiques de niveau recherche, publiés ou non, émanant des établissements d'enseignement et de recherche français ou étrangers, des laboratoires publics ou privés.

Dual-band LSPR of tungsten bronze nanocrystals tunable over NIR and SWIR ranges

Yannis Cheref¹, Florian Lochon², Louise Daugas¹, Capucine Cleret de Langavant¹, Éric Larquet¹, Alexandre Baron², Thierry Gacoin¹, Jongwook Kim^{1}*

¹Laboratoire de Physique de la Matière Condensée, CNRS, École Polytechnique, Institut Polytechnique de Paris, 91128 Palaiseau, France

²Univ. Bordeaux, CNRS, Centre de Recherche Paul Pascal, UMR5031, 33600, Pessac, France

ABSTRACT: The optical range of localized surface plasmon resonances (LSPR) has been extended over the infrared region by using doped semiconductor nanocrystals as hosting materials. The variable free carrier density and large variety of compositions of semiconductors have provided new methodologies to tune the LSPR wavelength. However, the tuning of the LSPR by controlling the anisotropic morphology of nanoparticles remains poorly explored with semiconductor hosts. And there is a lack of material with finely tunable LSPR in the near infrared (NIR) and short-wavelength infrared (SWIR) regions that is particularly interesting for applications to energy, imaging, telecommunication, and biomedical technologies. Here, we present synthetic methods to tailor the morphology of cesium-doped hexagonal tungsten bronze (Cs-HTB) nanocrystals exhibiting strong multi-band LSPR depending sensitively on the aspect

ratio (AR) of the particles. The LSPR band-splitting behavior is quantitatively analyzed as a function of the AR from 0.5 (platelets) to 6.2 (rods). Computational modelling, taking into account the anisotropic dielectric function of Cs-HTB, coincides unambiguously with the experiments confirming the dominant effect of both the shape and crystalline anisotropies on LSPR. The wide range of controllable ARs enables the LSPR of a single material composition to span the entire NIR-SWIR region. We demonstrate that these highly tunable plasmonic nanocrystals can be used to customize the solar irradiance through windows in order to optimize the efficiency of energy consumption in buildings.

INTRODUCTION

Since their discovery two decades ago, nanoparticles of degenerately doped semiconductors exhibiting Localized Surface Plasmon Resonances (LSPR) have sparked interest for applications because they exhibit resonances beyond the visible spectrum^[1]. We owe this property to their tunable free charge carrier densities that are typically lower than that of the well-known visible-light-absorbing noble metal nanoparticles. Ranging from 10^{18} to 10^{22} cm^{-3} , they induce plasmonic light absorption bands extending from visible red to mid-infrared (IR) light^[2].

Especially, the near infrared (NIR: 700 ~ 1400 nm) and short-wavelength infrared (SWIR: 1400 ~ 3000 nm) ranges is of great importance for energy and environmental issues^{[3][4][5][6]} as well as for imaging and biomedical applications^{[7][8][9]}, because half of the solar energy is radiated in the NIR-SWIR range which is also the transparency window for biological tissues.

Fine tuning of LSPR properties to cover specific wavelength ranges by playing on doping levels has been the focus of many recent studies. This has been achieved through control of non-

stoichiometry^{[10][2][11][12][13]}, aliovalent and interstitial doping^{[1][14][15][16][17][18]}, cation-anion co-doping^{[19][20][21]}, or dopant distribution inside the particle^{[22][23][24]}. Tunability ranges have been however limited by the active dopant density integrable in the host lattice. As an example, the LSPR absorption of tin-doped indium oxide (ITO) nanocrystals can be tuned from 1500 nm to mid-infrared range. However, the lowest wavelength is limited at 1500 nm as the absorption band redshifts back for Sn doping ratios above 10 % due to electron trapping around the Sn dopants^[15]. Moreover, because the doping level also determines the extinction cross section, it cannot be independently maximized at the same time as tuning the optimal wavelength of extinction.

Playing on the nanoparticle morphology is another classical way to tune the LSPR properties. In noble metal nanoparticles with intrinsically fixed carrier concentration, LSPR tuning has been achieved only by synthesizing nanoparticles in a variety of different shapes^{[25][26][27]} or by alloying different metals^[28]. For simple anisotropic morphologies such as nanorods, the absorption band splits into an almost fixed transverse mode band and a longitudinal mode band with a largely tunable wavelength that scales with the nanorod aspect ratio (AR)^[25]. When AR of gold nanorods, defined as the rod's length divided by its diameter, increases from 1 to 44, the peak of the longitudinal mode band redshifts from 500 nm to 2500 nm^[29]. However, due to the transverse mode band being fixed in the visible range, gold nanorods are suboptimal for use in IR-selective applications when optical transparency in the visible range needs to be preserved.

Due to their potential for optical and optoelectronic devices, methods to produce semiconductor nanocrystals in various shapes have been developed, from spheres and regular polyhedra to complex multi-material multipods^{[30][31][32][33][34][21][35][18][36]}. The LSPR properties of such complex shapes in materials other than noble metals are scarce and show that some of them

exhibit behaviors that are different from those of noble metal nanoparticles. For instance, metal chalcogenide nanorods or multipods exhibit only a single LSPR band along a certain crystalline axis^[37]. In the case of cesium-doped hexagonal tungsten bronze (Cs-HTB: Cs_xWO_{3-y} with $0 < x < 0.33$ and $0 < y < 0.3$) nanoprisms, the morphology-driven LSPR band splitting can be compensated by the effect of intrinsic crystalline anisotropy^[38]. These pioneering studies propose an advanced tunability in LSPR through the control of complex and highly anisotropic crystalline structures of semiconductors. However, fine control of the morphology of plasmonic non-metal nanocrystals, such as AR-selective synthesis of nanorods, is still a challenge. In the previous work on Cs-HTB nanocrystals^[38], the samples with different shapes were obtained only in a limited AR range without a reliable control of the synthesis. It is thus highly desirable, for a selected material composition, to develop a reproducible synthetic protocol ensuring an exquisite control of particle shape followed by a systematic study of the shape-dependent LSPR response.

This study aims to finely control the morphology of doped semiconductor nanocrystals extending the LSPR tunability over the entire NIR-SWIR range. We carried out our investigation using tungsten oxides compounds known to absorb in the Visible-NIR range. They are already used for solar-shielding applications^{[39][3][40][41]}. We focus on Cs-HTB, which presents both a high crystalline anisotropy owed to its hexagonal crystal structure, and a high NIR selectivity, as it maintains a high visible-range transmittance^[42] desirable for various optical applications. We demonstrate reproducible synthesis protocols of Cs-HTB nanocrystals with a fine control of the size and aspect ratio over a largely extended AR range from 0.5 to 6.2, far beyond the maximum AR of 1.8 reported previously by Kim *et al*^[38]. Quantitative evolutions of the LSPR split-bands across the entire NIR-SWIR range as a function of AR is presented. The highly anisotropic morphology of nanocrystals allowed to revisit the LSPR band-splitting effect induced by

cooperation of crystalline and shape anisotropies, and to experimentally observe a unique behavior of LSPR band-crossover at $AR \sim 2$. Our computational simulation based on the Drude model adapted in anisotropic dielectric media coincides very well with the observed LSPR behavior and assesses quantitatively the relative contributions of damped oscillation and the particle polydispersity on the broadening of LSPR bands.

RESULT & DISCUSSION

Synthesis. Cs-HTB nanocrystals with various sizes and aspect ratios were synthesized by modifying several experimental parameters of the previously reported thermal decomposition process^{[33][38][41]}. The initial process was a hot injection of a degassed solution of WCl_4 in Oleic Acid (OA) into a degassed solution of CsCl in OA pre-heated at 300 °C, with the final tungsten concentration of 0.02 mol/L and the Cs/W molar ratio of 0.6. This process was first changed by lowering the Cs/W molar ratio to 0.33, yielding nanocrystals with $AR = 0.5$ (4.7 nm \times 9.8 nm) and by increasing it to 6, yielding to $AR = 0.8$ (10.4 nm \times 13.4 nm). It was found that a large amount of CsCl salts precipitated during the synthesis, which would have limited the availability of Cs toward the formation of Cs-HTB. As this could be a reason for the limitation of morphology control even with a large excess of Cs ratio, tungsten hexacarbonyl ($W(CO)_6$) and cesium carbonate (Cs_2CO_3) were used as reactants in order to avoid the unwanted crystallization of CsCl. The necessary Cs/W ratio was then dramatically reduced below 0.33 implying an efficient incorporation of Cs into the oxide lattice. In this condition, by reducing the Cs/W ratio down to 0.15 and also the concentration of tungsten to 0.02 mol/L, Cs-HTB nanocrystals with good monodispersity and dispersion quality were obtained presumably diminishing supersaturation of the reactants and favoring nanocrystal growth over nucleation. When applied in a heat-up process, these new precursors enabled producing rod-shaped particles with a

moderate AR of 1.8 (12.9 nm × 7.4 nm). Longer nanorods with AR = 2.9 (54.3 nm × 18.5 nm) were obtained when the concentrations of the reactants were further decreased to 0.35 mmol/L in cesium. Even longer nanorods with AR = 4.5 (44.8 nm × 9.6 nm) and 6.2 (31.8 nm × 5.3 nm) were obtained in a hot injection process with the Cl-free precursors.

Particle Morphology. The transmission electron microscopy (TEM) images (**Fig. 1**) show consistent monocrystalline features and hexagonal prism shapes for all the synthesized particles, while their ARs are significantly different from one to the others. One can see the natural tendency of the particles lying with their longer axis parallel to the TEM grid (**Fig. 1**). Thus, the hexagonal basal plane is more visible for AR < 1 (**Fig. 1a-b**) and the rectangular prismatic plane is more visible for AR > 1 (**Fig. 1c-f**). Note that the hexagonally packed particles in the corner of **Fig. 1c** are also short rods with the same AR as the surrounding rods, which is evidenced by the darker contrast of this region. The high-resolution TEM images (**Fig. 1g**) clearly show the lattice structure of Cs-HTB in the prismatic and basal planes, which is schematized in **Fig. 1h**. The particle dimensions (length and width) were measured on more than two hundred particles for each sample on multiple TEM images, of which the average values and their standard deviations (σ) are presented in **Table 1**. A large size distribution is detrimental to the investigation of the optical LSPR band splitting phenomenon, as it enlarges the band width of each mode – transverse or longitudinal – and merges them. The σ values of our samples are comprised between 17 ~ 40 % of the mean values. The histograms in **Fig. S1** and the scatterplots in **Fig. 1i** show that they correspond to a single population for one sample that is distinct to each other. Such levels of monodispersity were sufficient for quantitative analyses of the position and width of separate LSPR bands (see next section). The X-ray diffraction (XRD) patterns for AR=0.4 (**Fig. 1j**) and AR = 6.2 (**Fig. 1k**) both confirm the Cs-HTB phase, while the cubic CsCl phase

coexists for AR=0.4 as unwanted byproduct harming the stoichiometric control while using chloride precursors. This CsCl residue could easily be removed by purification. The intense peaks for AR = 6.2 at 2θ of 23.397° (002) and of 47.848° (004) indicate a strong tendency of the in-plane alignment of the long nanorods on the substrate as seen in the TEM image (**Fig. 1f**).

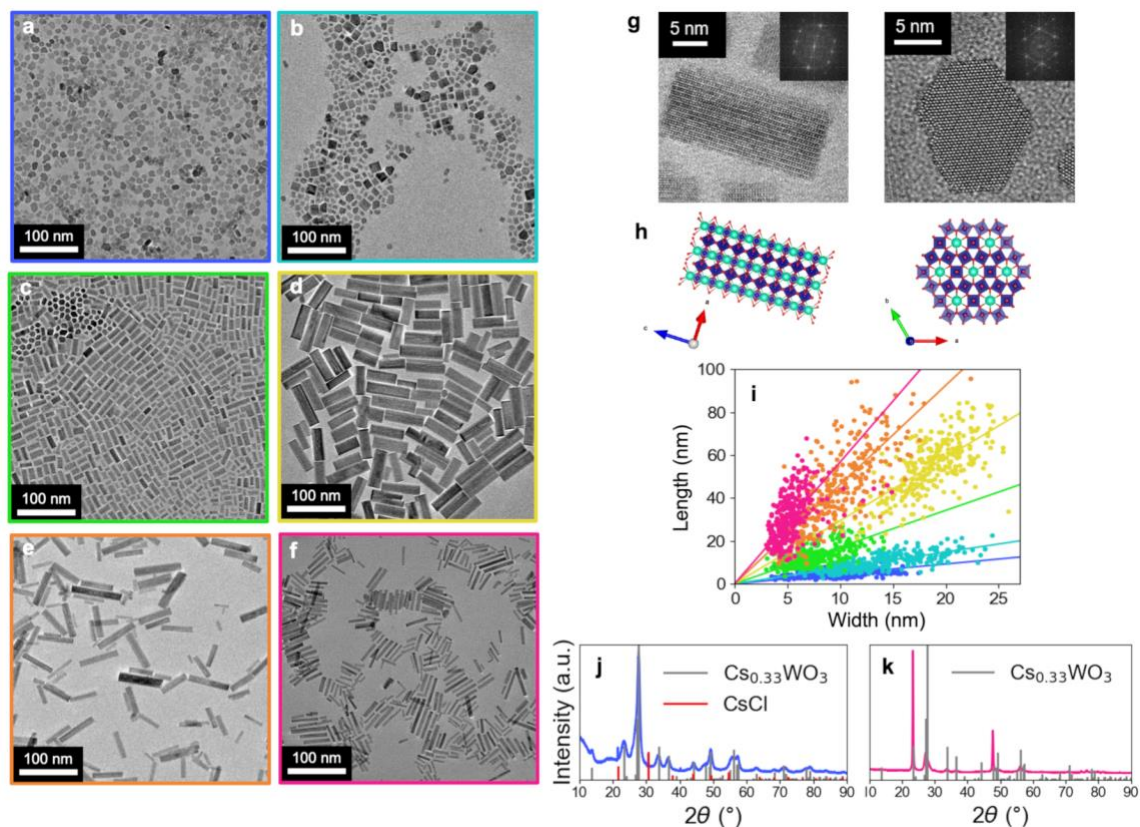


Figure 1. Cs-HTB nanocrystals with varied aspect ratios. (a-f) TEM images of the Cs-HTB nanocrystal samples A (AR = 0.5; a), B (AR = 0.8; b), C (AR = 1.8; c), D (AR = 2.9; d), E (AR = 4.6; e) and F (AR = 6.2; f) (g) High-resolution TEM images showing the lattice structure of the prismatic plane (left; from the sample C) and the basal plane (right; from the sample B). (h) Illustration of the Cs-HTB lattice structure projections on the prismatic plane and the basal plane. The cesium sites are colored in green, the tungsten sites in blue and oxygens in red. (i) Scatterplots of the size distribution for each AR.

(j-k) X-ray diffraction (XRD) patterns of the samples A (j) and F (k) and the corresponding hexagonal $\text{Cs}_{0.32}\text{WO}_3$ (JCPDS 1524692) and CsCl (JCPDS 9008789) reference patterns.

	AR	Length (nm)		Width (nm)	
A	0.5	4.7 ± 1.4	(30%)	9.9 ± 2.6	(26%)
B	0.8	10.4 ± 4.1	(39 %)	13.4 ± 4.0	(30 %)
C	1.8	12.9 ± 4.7	(36 %)	7.4 ± 2.3	(31 %)
D	2.9	54.3 ± 13.4	(25 %)	18.5 ± 3.2	(17 %)
E	4.6	44.8 ± 17.9	(40 %)	9.7 ± 3.1	(32 %)
F	6.2	31.8 ± 11.0	(35 %)	5.3 ± 1.6	(30 %)

Table 1. Summary of the average dimensions of the different synthesized batches of Cs-HTB nanoparticles, with standard deviations (σ) given both in nm and in percentage.

Light extinction by LSPR. The LSPR of the Cs-HTB nanocrystals manifests as strong light extinction at their resonance energies in the NIR-SWIR range. The AR-dependent evolution of the LSPR extinction spectra was observed in the full Vis-NIR-SWIR range (400 nm to 3000 nm) (**Fig. 2a**). It is clearly seen that the spectral line shape of the LSPR varies with the AR of the particles over a wide region covering the entire NIR-SWIR range, and even beyond for the high AR of 6.2 covering partially the mid-infrared range (>3000 nm). As mentioned above, this behavior originates from the AR-dependent band-splitting of LSPR exhibiting the two transverse and longitudinal modes. In order to obtain quantitative data on the width and position of the

different peaks, the experimental spectra were deconvoluted by fitting with pseudo-Voigt functions (**Fig. 2b-e**). The typical bandwidths for both transverse and longitudinal modes were found to be 0.53 ± 0.08 eV with a quality factor (Q-factor: resonance frequency/bandwidth) of 1.69 ± 0.46 , which is roughly 8 times and 2 times lower than those of gold nanoparticles^[43] and ITO nanocrystals respectively^[44]. We attribute this moderate quality of resonance mostly to a number of damping processes related to the nanocrystals' defects on surface and internal volume^[45] as well as to the intrinsic optical constants of the Cs-HTB^[38]. The overall wavelength and amplitude of LSPR is a function of the doping levels noted as x and y values in the Cs_xWO_{3-y} composition. The concentration of Cs-dopants was measured by ICP-OES (inductively coupled plasma – optical emission spectroscopy), which was variable among the samples in the range of $x = 0.18 \sim 0.32$ without correlation with the particle AR. The concentration of oxygen vacancies (providing 2 electrons per 1 vacancy site) was estimated to be $y = 0.2 \sim 0.3$ from the fully reduced state of Cs-HTB after the synthesis in the anaerobic condition. An exceptionally high free electron density of $e^-/W = 0.6 \sim 0.9$ ($\sim 10^{21}$ cm⁻³) can thus be achieved in Cs-HTB allowing the LSPR in NIR-SWIR.

For AR = 0.5 and 0.8 (**Fig. 2a** blue and light blue curves), the two main separate bands are visible, and the deconvoluted peaks are found to be centered at 1.65 eV/0.83 eV and 1.43 eV/0.93 eV respectively (**Fig. 2b**). It is also clear for AR = 4.6 and 6.2 (**Fig. 2a** orange and pink curves) that the two main bands are separated at 0.55 eV/0.94 eV and 0.47 eV/0.98 eV (**Fig. 2e**). The two other spectra for AR = 1.8 and 2.9 (**Fig. 2c-d**-green and yellow curves) feature almost single bands with their maxima near 0.9 eV. However, the visible peak shoulder for AR = 2.9 near 1 eV hints that there exist two main bands that are merged together. Our experimental spectra obtained for AR = 0.8 and 1.8 are in agreement with the previous finding by Kim *et*

al.^[38], which showed that the higher-energy band at small ARs corresponded to a longitudinal LSPR mode. As AR was increased up to 1.8, this mode redshifted to overlap with the transverse mode fixed at around 1 eV. It could be predicted from this previous study that, if the AR was further increased, the longitudinal mode would cross over the transverse mode and appear at an energy lower than 1 eV. This prediction is confirmed with our new result with the elongated nanorods with AR up to 6.2, for which the first peak stays near 1eV and the second peak was largely redshifted to 0.47 eV (**Fig. 2e**). The deconvolution of the two intermediary samples (AR = 1.8 and 2.9) were conducted following the assumption that the transverse mode was almost fixed while the longitudinal mode largely redshifted with increasing AR. The centers of the deconvoluted peaks obtained in this way are found at 0.92 eV and 0.93 eV for AR = 1.8 (**Fig. 2c**), and at 0.71 eV and 1.03 eV for AR = 2.9 (**Fig. 2d**). Therefore, when attributing the almost fixed peak near 1eV to the transverse mode, the other peak, the longitudinal mode, continuously redshifts from 1.65 eV to 0.47 eV when AR increases from 0.5 to 6.2. This is the first experimental observation of such an LSPR band-crossover at $AR \neq 1$, which can be manifested only with the LSPR hosts possessing highly anisotropic crystalline structures and dielectric functions.

Three contributions were often necessary to accurately fit the experimental spectra with two main bands and an additional band that is less intense and located at higher energy (grey lines in **Fig. 2c-e**). Considering its position and intensity, we attribute this small additional band to the volume symmetric mode of the LSPR that resonates at lower wavelengths and exhibits larger losses than the surface anti-symmetric modes. The coexistence of these surface and volume modes was confirmed by a computational study discussed below.

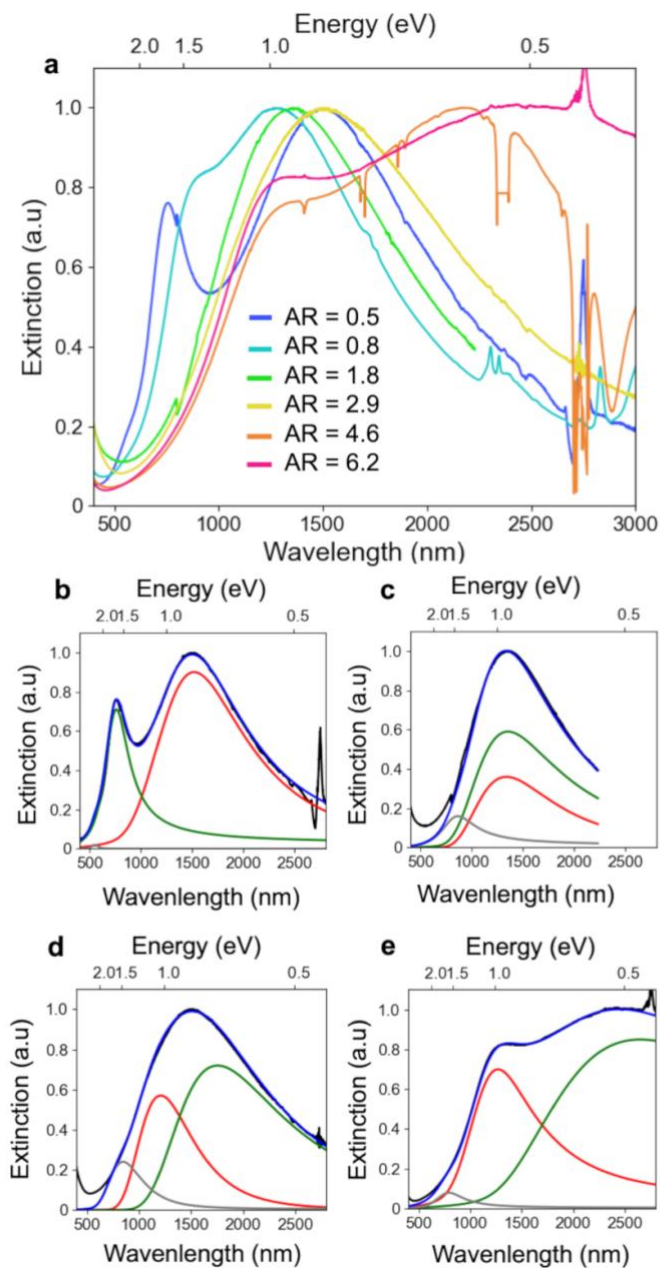


Figure 2. LSPR light extinction by Cs-HTB nanocrystals. (a) The light extinction spectra of the colloidal Cs-HTB nanocrystals with varied aspect ratios corresponding to the sample A-F seen in Fig. 1. (b-e) Deconvolution peak analysis featuring the measured spectra (black lines), three deconvoluted peaks (red, grey and green lines), and the sum of the three deconvoluted peaks (blue lines) for the samples A (b), C (c), D (d) and F (e).

Simulation of LSPR extinction. In order to theoretically investigate the observed LSPR band-splitting phenomenon, the absorption and scattering cross-sections were calculated using the finite-element method based commercial software COMSOL Multiphysics (the detail of the modelling approach is described in the S.I.). Light scattering was found to be negligible compared to the absorption for the size range of the studied nanocrystals. The numerical particles have a hexagonal basal plane for which the radius of the circle circumscribed to the hexagon is R and the length along the c-axis is L (**Fig. 3b**). The vertices and edges are rounded to avoid singularities when meshing the model. In order to consider the influence of crystalline anisotropy of Cs-HTB, an anisotropic uniaxial tensor is used to define the permittivity of the nanocrystals. The ordinary permittivity ε_o is that of the transverse cross-section, while the extraordinary permittivity ε_e is that of the longitudinal axis. Both $\varepsilon_{o,e}$ are defined by a Drude model taken from the previous report on Cs-HTB^[38]. The plasma (ω_p) and damping frequency (γ) are the two notable parameters of the Drude model.

The spectral variations of the extinction cross-section, $\sigma_e(\lambda)$, are shown in **Fig. 3a** for all the ARs investigated following the experimental dimensions and taking polydispersity into account (**Table 1**). These series of extinction spectra exhibit two major peaks, one corresponding to the main resonance peak under the longitudinal mode and the other one for the transverse mode. The peak centers of both longitudinal and transverse resonances are plotted as a function of AR and are compared to the experimentally retrieved values (**Fig. 3c**). As can be seen, the longitudinal band is largely red-shifted when the AR is increased, while the transverse band shows a moderate blue-shift from approximately 0.9 eV to 1.1 eV. A band crossover between the longitudinal and transverse mode bands is observed at an energy near 1 eV for AR = 1.8. This excellent agreement between the experiment and the theoretical simulation validates the

deconvolution method adopted (**Fig. 2b-e**) and also our numerical model for Cs-HTB nanorods. We attribute the discrepancy between the experiments and simulation to the uncertainty in the spectral deconvolution analysis when the two main bands are overlapping and broadening when increasing the AR.

Our preliminary model taking into account the statistical distribution of particle dimensions (**Table 1**) and the damping constants (γ) from the literature^[46] provided LSPR spectra much narrower than the experimental spectra (**Fig. S2**). We then performed a fitting analysis adjusting for γ in the model (**Fig. S3** and **Table S2**) and found that the simulated LSPR spectra with somewhat increased γ (**Fig. 3a**) compare well to the experimental spectra (**Fig. 2a**). The deconvoluted spectra of simulated longitudinal and transverse modes (**Fig. S4**) also correspond to the experimental ones (**Fig. 2b-e**) although the relative peak intensities are not quantitatively the same. The damping effect larger than those in bulk Cs-HTB crystal are thus mainly responsible for the broad LSPR bandwidths and moderate Q-factors as described above. The polydispersity in particle dimensions is small enough to have a minor contribution. The γ values obtained by the fitting analysis are several times larger than that of ITO nanoparticles (1850 cm^{-1})^[23], which is also consistent with the moderate light extinction cross-section $\sigma_e(\lambda_{peak})$ of $7\sim 18 \mu\text{m}^{-1}$ measured with the Cs-HTB nanocrystals in comparison to those of ITO ($50 \mu\text{m}^{-1}$)^[47].

The simulated longitudinal band contains two different modes at different wavelengths (**Fig. S5**). One is a volume mode that has stronger localization in the core of the particle, and the second one is a surface mode stronger at the particle edges. The surface mode is predominant for $AR > 1$ because it exhibits smaller losses than the volume mode. This is due to the fact that it exhibits a zero of the electric field in the center on the nanorod axis^[48]. The volume mode has a higher energy than the surface mode with a moderate intensity, which could thus be responsible for the

small additional contribution at high-energy found from the experimental LSPR spectra (**Fig. 2c-e**).

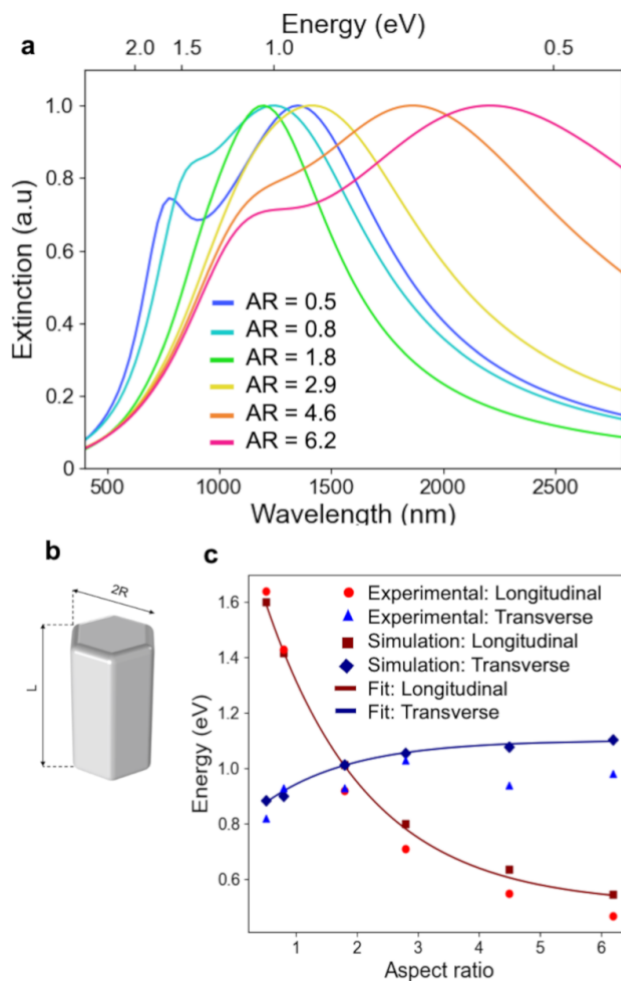


Figure 3. Simulation of the LSPR extinction of Cs-HTB nanocrystals. (a) Spectral variations of the normalized extinction cross-section σ_{ext} of simulated nanorods for various aspect ratios (AR). The corresponding dimensions are those of Table 1. (b) Illustration of the nanorod model used in the finite-element method simulations. (c) Comparison between the retrieved resonance energies of the experimental and simulated longitudinal and transverse modes as a function of AR. The lines are fitting curves of the points of simulation.

Efficiency of selective solar NIR shielding. While the LSPR amplitude is dampened in Cs-HTB due to the relatively low quality factor, the spreading of its spectrum as a result can be a useful trade-off for certain applications requiring a wide spectral coverage. For instance, the NIR part of solar irradiation spans from 700 to 2500 nm (**Fig. 4** grey line), which is desired to be blocked through building windows to improve the efficiency of energy consumption. Diverse tungsten oxide-based compounds have been used to tint windows either by their plasmonic or polaronic light extinction properties depending on their structures^{[3][42]}. The tunable LSPR spectra of the Cs-HTB nanocrystals with variable ARs enable finely customizing the solar transmission filtered through them. Assuming that the nanocrystals deposited as tint exhibit the same optical absorption as in colloidal solutions, the products of the LSPR spectra with the solar radiation spectrum can provide estimation of the NIR shielding performance (**Fig. 4** colored lines). These product spectra reveal that the ratio of the solar transmissions in the Vis and NIR ranges are sensitive to the AR of the particles. The solar energy transmittance selectivity (SETS)^[49] figuring the NIR-to-Vis transmittance ratio was the highest for AR=1.8 and AR = 6.2 (**Table 2**), which is thus ideal particles for a window tint material most efficiently blocking the solar heat gain through NIR maintaining high Vis-transparency. The A_{NIR} values in **Table 2** indicate the percentage of NIR-absorption for a fixed Vis-transmittance of 80%. (The mathematical definition of SETS and A_{NIR} can be found in the S.I.). In general, an optimal AR can be chosen depending on the climate condition and the lighting/heating/air-conditioning loads for each different application. The necessary thickness of the Cs-HTB nanocrystal film to achieve 80% solar NIR absorption is calculated to be only a few hundreds of nanometers by virtue of the strong extinction coefficient of Cs-HTB thanks to the resonance of plasmonic effect. In order to realize the provided SETS, it is necessary to avoid the LSPR coupling effect causing spectral

broadening and dampening when particles approach closely to each other. A solution is to embed the dispersed particles in a transparent dielectric matrix, which is beyond the scope of this paper while is our ongoing project.

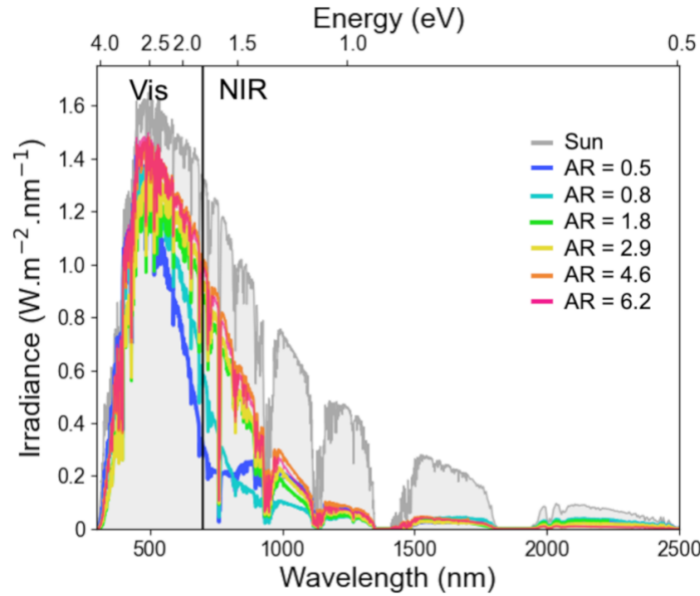


Figure 4. Solar transmission spectra filtered by Cs-HTB nanocrystals. (grey line) Solar irradiance at sea level. (colored lines) Absorption spectra of Cs-HTB shown in **Fig. 2a** convoluted with the solar spectrum at sea level.

AR	0.5	0.8	1.8	2.9	4.6	6.2
SETS	0.62	0.72	0.76	0.71	0.75	0.76
A_{NIR} (%)	44	63	72	62	70	72

Table 2. Solar energy transmittance selectivity (SETS) between Vis/NIR ranges and the percentage of NIR absorption for 80% Vis-transmittance of Cs-HTB nanocrystals with varied aspect ratios.

CONCLUSION

We have developed colloidal synthesis protocols of Cs-HTB nanocrystals to achieve morphology-dependent tunability of LSPR properties. An exquisite control of the size and aspect ratio of the nanocrystals enable tailoring the dual-band LSPR across the entire near infrared (NIR) and short-wavelength infrared (SWIR) ranges with a single material composition. We have shown that combining the anisotropies in shape and crystal structure enables a crossover of the split bands when the particle is far from isotropic in its shape. This is indeed a unique characteristic of anisotropically structured nanocrystals which does not appear in metallic systems. The computational simulations based on the Drude model with the anisotropic dielectric functions of Cs-HTB have confirmed the experimentally observed LSPR band-splitting behavior. The blue- and red-shifts of the transverse- and longitudinal modes as a function of the particle aspect ratio proves that the optical response of our Cs-HTB nanocrystals is entirely a plasmonic behavior (i.e. collective oscillations of delocalized electrons). This is also evidenced by its naturally high doping level ($x = 0.18 \sim 0.32$ and $y = 0.2 \sim 0.3$ for $\text{Cs}_x\text{WO}_{3-y}$) and thereby achieved abundance of electron density ($\sim 10^{21} \text{ cm}^{-3}$) for which diverse tungsten oxide matrices have been analyzed to be in metallic states^{[50][51][52]}. The extended tunability of dual-band LSPR demonstrated in this work provides novel strategies to design various optical systems capable of coupling with LSPRs in multiple and wide wavelength ranges. As an example, we provided a quantitative assessment of the NIR-selective solar shielding performance for applications to energy saving. The dual-band feature of the anisotropic $\text{Cs}_x\text{WO}_{3-y}$ nanocrystals can be used both separately or together based on the methods to control the polarization or near-field coupling.

MATERIALS & METHODS

Synthesis of Cs-HTB nanocrystals. Standard Schlenk line technique under nitrogen and vacuum was used. Oleic acid (technical grade, 90% from Sigma Aldrich) was used as solvent and degassed for 3 hours at 120°C before synthesis. For nanoplatelets, 652 mg (2 mmol) WCl_4 (Sigma Aldrich) is mixed with 10 mL of oleic acid (0.2M) and degassed during 30 minutes at 120°C to form W-oleate precursor. In separate flasks, 56 mg (0.33 mmol) and 1060 mg (6 mmol) of CsCl (Sigma Aldrich) were mixed with 45 mL of oleic acid for AR = 0.5 and AR = 0.8 respectively. The mixture was degassed for 30 minutes at 120°C, heated to 300°C under nitrogen atmosphere, and then 5 mL (1mmol) of the W-oleate solution was quickly injected. For nanorods, Cs-oleate precursor was prepared by degassing a 0.2M solution of Cs_2CO_3 (Sigma Aldrich) in oleic acid at 120°C for 30 minutes. For AR = 1.8 and 2.9, 156 mg (0.44mmol) of $W(CO)_6$ (Sigma Aldrich) and 73 μ L (0.015 mmol) and 36.5 μ L (0.007mmol) of Cs-oleate solution were respectively mixed in 20 mL of oleic acid, degassed for 30 minutes, and then heated up to 300°C. For AR = 6.2, the W-oleate precursor was prepared by keeping a 10 mL solution of $W(CO)_6$ at 0.1 M in oleic acid at 180°C in an oil bath overnight under nitrogen flow. 1mL of this solution was injected in a 0.75 mM solution of Cs-oleate in oleic acid at 300°C. All reactions were kept at 300°C for 30 minutes, cooled down to room temperature and transferred into a glovebox with nitrogen atmosphere. The prepared nanocrystals were washed by centrifugation at 4000 rfc for 5 minutes several times and kept at a concentration of 10 mg/mL in toluene in the glovebox.

Characterizations. Transmission electron microscopy (TEM) and High-Resolution TEM (HR-TEM) were performed using JEOL JEM-2010F. Size analysis were performed using ImageJ software on more than two hundred particles for each sample. XRD patterns were measured with dropcasted nanocrystals on (400) oriented silicon wafers using a Bruker D8 Advance diffractometer with a Cu K α X-ray source operating at 40kV and 40mA between $2\theta=10^\circ \sim 90^\circ$ with a step size of 0.02° and a scan speed of 0.9 sec/step. Optical extinction spectra were obtained using Agilent-Cary5000 spectrophotometer with colloidal nanocrystal solutions using a quartz cuvette (1 cm optical path) with an airtight screw cap. For this, the nanocrystals were functionalized with mPEG5k-Si (methoxy-polyethylene-glycol silane with average molecular weight of 5000) in toluene with added acetic acid, and then dispersed in tetrachloroethylene. This functionalization allowed high colloidal dispersion stability and almost didn't affect the optical property. ICP-OES was performed using iCAP 6000 Thermo-Scientific.

Computational simulation. The scattered field formalism is used on an individual rod under plane-wave illumination. The numerical rods have a hexagonal transverse cross-section (see illustration on Fig. 3(a)). The radius of the circle circumscribed to the hexagon is R and the length of the rod is L . The vertices and edges are rounded to avoid singularities when meshing the model and to realistically account for the geometry observed empirically on the TEM images. An anisotropic uniaxial tensor is used to define the permittivity of the nanorod. The ordinary permittivity ϵ_o is that of the transverse cross-section, while the extraordinary permittivity ϵ_e is that of the longitudinal axis. Both $\epsilon_{o,e}$ are defined by a Drude model taken from^[38]. The refractive index of the medium surrounding the particle is set to 1.47 (index of TCE). The absorption cross-section σ_a is computed by integrating the ohmic losses in the particle and dividing it by the intensity of the excitation field, while the scattering cross-section σ_s is computed by calculating

the flux of the Poynting vector of the scattered-field across a closed sphere surrounding the nanorod. The extinction σ_e cross-section is computed using the optical theorem: $\sigma_e = \sigma_a + \sigma_s$. For each wavelength, the cross-sections are computed under two illumination configurations. The longitudinal (resp. transverse) configuration is that when the electric field of the external field is parallel to the long axis (resp. transverse hexagonal plane) of the rod. For each configuration, $\sigma_e^{L,T}$ are calculated, where the L and T superscripts refer to the longitudinal and transverse configurations respectively. A preliminary study was conducted to ensure that rotating the rod along the long axis only has a vanishingly weak effect on the computation of the cross-sections. To account for the experimental situation, averaging of the extinction cross-section was carried out over all rod orientations with respect to the incident field by using the following formula: $\sigma_e = 1/3 \sigma_e^L + 2/3 \sigma_e^T$.

ASSOCIATED CONTENT

Supplementary Information. Size analysis of nanocrystals, Computational LSPR simulation before adjusting the damping parameters, fitting analysis of the damping parameters, LSPR field distribution analysis, Calculation of solar energy transmittance selectivity. The Supporting Information is available free of charge on the ACS Publications website.

AUTHOR INFORMATION

Corresponding Author

* jong-wook.kim@polytechnique.edu

Author Contributions

Y.C., C.C-L., and L.D. performed synthesis, surface chemistry, and characterizations. F.L. and A.B. performed computational simulations. E.L. Y.C., C.C-L., and L.D. performed electron microscopy. Y.C., L.D., and J.K. prepared the manuscript. L.D. analyzed the data and prepared figures. J.K., A.B., and T.G. supervised the research and revised the manuscript. All authors have given approval to the final version of the manuscript.

Funding Sources

This work was supported by the French National Research Agency (ANR) in the frame of the projects Spectra (ANR-16-CE24-0014) and Plasmoglaz (ANR-18-CE05-0038).

ACKNOWLEDGMENT

The authors thank Dr. Sandrine Tusseau-Nenez for the XRD analysis and Dr. Jacques Peretti for the instrumentation of the spectrophotometry.

ABBREVIATIONS

OA, Oleic Acid; TEM, Transmission Electron Microscopy; XRD, X-Ray Diffraction.

REFERENCES

- [1] T. Nütz, U. Zum Felde, and M. Haase, "Wet-chemical synthesis of doped nanoparticles: Blue-colored colloids of n-doped SnO₂:Sb," *J. Chem. Phys.*, vol. 110, no. 24, pp. 12142–12150, 1999, doi: 10.1063/1.479151.
- [2] J. M. Luther, P. K. Jain, T. Ewers, and A. P. Alivisatos, "Localized surface plasmon resonances arising from free carriers in doped quantum dots," *Nat. Mater.*, vol. 10, no. 5, pp. 361–366, 2011, doi: 10.1038/nmat3004.

- [3] J. Kim *et al.*, “Nanocomposite Architecture for Rapid, Spectrally-Selective Electrochromic Modulation of Solar Transmittance,” *Nano Lett.*, vol. 15, no. 8, pp. 5574–5579, 2015, doi: 10.1021/acs.nanolett.5b02197.
- [4] A. Llordés, G. Garcia, J. Gazquez, and D. J. Milliron, “Tunable near-infrared and visible-light transmittance in nanocrystal-in-glass composites,” *Nature*, vol. 500, no. 7462, pp. 323–326, 2013, doi: 10.1038/nature12398.
- [5] K. Adachi, M. Miratsu, and T. Asahi, “Absorption and scattering of near-Infrared light by dispersed lanthanum hexaboride nanoparticles for solar control filters,” *J. Mater. Res.*, vol. 25, no. 3, pp. 510–521, 2010, doi: 10.1557/jmr.2010.0075.
- [6] G. Garcia, R. Buonsanti, A. Llordés, E. L. Runnerstrom, A. Bergerud, and D. J. Milliron, “Near-Infrared Spectrally Selective Plasmonic Electrochromic Thin Films,” *Adv. Opt. Mater.*, vol. 1, no. 3, pp. 215–220, 2013, doi: 10.1002/adom.201200051.
- [7] W. Guo, C. Guo, N. Zheng, T. Sun, and S. Liu, “CsxWO₃ Nanorods Coated with Polyelectrolyte Multilayers as a Multifunctional Nanomaterial for Bimodal Imaging-Guided Photothermal/Photodynamic Cancer Treatment,” *Adv. Mater.*, vol. 29, no. 4, 2017, doi: 10.1002/adma.201604157.
- [8] C. M. Hessel *et al.*, “Copper selenide nanocrystals for photothermal therapy,” *Nano Lett.*, vol. 11, no. 6, pp. 2560–2566, 2011, doi: 10.1021/nl201400z.
- [9] X. Liu, C. Lee, W. Law, D. Zhu, M. Liu, and M. Jeon, “Au–Cu_{2–x}Se Heterodimer Nanoparticles with Broad Localized Surface Plasmon Resonance as Contrast Agents for Deep Tissue Imaging,” 2013.
- [10] Y. Zhao, H. Pan, Y. Lou, X. Qiu, J. Zhu, and C. Burda, “Plasmonic Cu_{2–x}S nanocrystals: Optical and structural properties of copper-deficient copper(I) sulfides,” *J. Am. Chem. Soc.*, vol. 131, no. 12, pp. 4253–4261, 2009, doi: 10.1021/ja805655b.
- [11] D. Dorfs *et al.*, “Reversible tunability of the near-infrared valence band plasmon resonance in Cu_{2–x}Se nanocrystals,” *J. Am. Chem. Soc.*, vol. 133, no. 29, pp. 11175–11180, 2011, doi: 10.1021/ja2016284.
- [12] I. Kriegel *et al.*, “Tuning the excitonic and plasmonic properties of copper chalcogenide nanocrystals,” *J. Am. Chem. Soc.*, vol. 134, no. 3, pp. 1583–1590, 2012, doi: 10.1021/ja207798q.
- [13] K. Manthiram and A. P. Alivisatos, “Tunable localized surface plasmon resonances in tungsten oxide nanocrystals,” *J. Am. Chem. Soc.*, vol. 134, no. 9, pp. 3995–3998, 2012, doi: 10.1021/ja211363w.
- [14] S. D. Lounis, E. L. Runnerstrom, A. Llordés, and D. J. Milliron, “Defect chemistry and Plasmon physics of colloidal metal oxide Nanocrystals,” *J. Phys. Chem. Lett.*, vol. 5, no. 9, pp. 1564–1574, 2014, doi: 10.1021/jz500440e.
- [15] M. Kanehara, H. Koike, T. Yoshinaga, and T. Teranishi, “Indium tin oxide nanoparticles with compositionally tunable surface plasmon resonance frequencies in the near-IR region,” *J. Am. Chem. Soc.*, vol. 131, no. 49, pp. 17736–17737, 2009, doi: 10.1021/ja9064415.
- [16] D. J. Rowe, J. S. Jeong, K. A. Mkhoyan, and U. R. Kortshagen, “Phosphorus-doped silicon nanocrystals exhibiting mid-infrared localized surface plasmon resonance,” *Nano Lett.*, vol. 13, no. 3, pp. 1317–1322, 2013, doi: 10.1021/nl4001184.

- [17] B. Tandon, S. Ghosh, and D. J. Milliron, "Dopant Selection Strategy for High-Quality Factor Localized Surface Plasmon Resonance from Doped Metal Oxide Nanocrystals," *Chem. Mater.*, vol. 31, no. 18, pp. 7752–7760, 2019, doi: 10.1021/acs.chemmater.9b02917.
- [18] H. K. D. Le *et al.*, "Effects of I₂ on Cu_{2-x}S Nanoparticles: Enabling Cation Exchange but Complicating Plasmonics," *ACS Mater. Lett.*, vol. 2, no. 2, pp. 140–146, 2020, doi: 10.1021/acsmaterialslett.9b00402.
- [19] X. Ye, J. Fei, B. T. Diroll, T. Paik, and C. B. Murray, "Expanding the spectral tunability of plasmonic resonances in doped metal-oxide nanocrystals through cooperative cation-anion codoping," *J. Am. Chem. Soc.*, vol. 136, no. 33, pp. 11680–11686, 2014, doi: 10.1021/ja5039903.
- [20] R. Giannuzzi *et al.*, "Tunable Near-Infrared Localized Surface Plasmon Resonance of F, In-Codoped CdO Nanocrystals," *ACS Appl. Mater. Interfaces*, vol. 11, no. 43, pp. 39921–39929, 2019, doi: 10.1021/acsami.9b12890.
- [21] S. H. Cho *et al.*, "Spectrally tunable infrared plasmonic F,Sn:In₂O₃ nanocrystal cubes," *J. Chem. Phys.*, vol. 152, no. 1, 2020, doi: 10.1063/1.5139050.
- [22] S. D. Lounis, E. L. Runnerstrom, A. Bergerud, D. Nordlund, and D. J. Milliron, "Influence of dopant distribution on the plasmonic properties of indium tin oxide nanocrystals," *J. Am. Chem. Soc.*, vol. 136, no. 19, pp. 7110–7116, 2014, doi: 10.1021/ja502541z.
- [23] B. M. Crockett, A. W. Jansons, K. M. Koskela, D. W. Johnson, and J. E. Hutchison, "Radial Dopant Placement for Tuning Plasmonic Properties in Metal Oxide Nanocrystals," *ACS Nano*, vol. 11, no. 8, pp. 7719–7728, 2017, doi: 10.1021/acsnano.7b01053.
- [24] N. B. Saleh, D. J. Milliron, N. Aich, L. E. Katz, H. M. Liljestrand, and M. J. Kirišits, "Importance of doping, dopant distribution, and defects on electronic band structure alteration of metal oxide nanoparticles: Implications for reactive oxygen species," *Sci. Total Environ.*, vol. 568, pp. 926–932, 2016, doi: 10.1016/j.scitotenv.2016.06.145.
- [25] K. L. Kelly, E. Coronado, L. L. Zhao, and G. C. Schatz, "The Optical Properties of Metal Nanoparticles: The Influence of Size, Shape, and Dielectric Environment," *J. Phys. Chem. B*, vol. 107, no. 3, pp. 668–677, Jan. 2003, doi: 10.1021/jp026731y.
- [26] M. Grzelczak, J. Pérez-Juste, P. Mulvaney, and L. M. Liz-Marzán, "Shape control in gold nanoparticle synthesis," *Chem. Soc. Rev.*, vol. 37, no. 9, pp. 1783–1791, 2008, doi: 10.1039/b711490g.
- [27] S. S. Chang, C. W. Shih, C. D. Chen, W. C. Lai, and C. R. C. Wang, "The Shape Transition of Gold Nanorods," *Langmuir*, vol. 15, no. 3, pp. 701–709, 1999, doi: 10.1021/la980929l.
- [28] S. Ristig *et al.*, "Nanostructure of wet-chemically prepared, polymer-stabilized silver-gold nanoalloys (6 nm) over the entire composition range," *J. Mater. Chem. B*, vol. 3, no. 23, pp. 4654–4662, 2015, doi: 10.1039/c5tb00644a.
- [29] S. Link and M. A. El-Sayed, "Simulation of the optical absorption spectra of gold nanorods as a function of their aspect ratio and the effect of the medium dielectric constant (Journal of Physical Chemistry B (1999) 103B)," *J. Phys. Chem. B*, vol. 109, no. 20, pp. 10531–10532, 2005, doi: 10.1021/jp058091f.

- [30] L. Manna, E. C. Scher, and A. P. Alivisatos, "Synthesis of soluble and processable rod-, arrow-, teardrop-, and tetrapod-shaped CdSe nanocrystals," *J. Am. Chem. Soc.*, vol. 122, no. 51, pp. 12700–12706, 2000, doi: 10.1021/ja003055+.
- [31] X. Wang, J. Zhuang, Q. Peng, and Y. Li, "A general strategy for nanocrystal synthesis," *Nature*, vol. 437, no. 7055, pp. 121–124, 2005, doi: 10.1038/nature03968.
- [32] M. V. Kovalenko *et al.*, "Prospects of nanoscience with nanocrystals," *ACS Nano*, vol. 9, no. 2, pp. 1012–1057, 2015, doi: 10.1021/nn506223h.
- [33] T. M. Mattox, A. Bergerud, A. Agrawal, and D. J. Milliron, "Influence of shape on the surface plasmon resonance of tungsten bronze nanocrystals," *Chem. Mater.*, vol. 26, no. 5, pp. 1779–1784, 2014, doi: 10.1021/cm4030638.
- [34] T. R. Gordon *et al.*, "Shape-dependent plasmonic response and directed self-assembly in a new semiconductor building block, indium-doped cadmium oxide (ICO)," *Nano Lett.*, vol. 13, no. 6, pp. 2857–2863, 2013, doi: 10.1021/nl4012003.
- [35] R. M. Córdova-Castro *et al.*, "Anisotropic Plasmonic CuS Nanocrystals as a Natural Electronic Material with Hyperbolic Optical Dispersion," *ACS Nano*, 2019, doi: 10.1021/acsnano.9b00282.
- [36] G. Liu, F. Kong, J. Xu, and R. Li, "Novel synthesis of 0D, 1D and 2D nano-CsxWO3 and their tunable optical-thermal response performance," *J. Mater. Chem. C*, vol. 8, no. 30, pp. 10342–10351, 2020, doi: 10.1039/d0tc01254h.
- [37] Y. W. Jun, J. S. Choi, and J. Cheon, "Shape control of semiconductor and metal oxide nanocrystals through nonhydrolytic colloidal routes," *Angew. Chemie - Int. Ed.*, vol. 45, no. 21, pp. 3414–3439, 2006, doi: 10.1002/anie.200503821.
- [38] J. Kim, A. Agrawal, F. Krieg, A. Bergerud, and D. J. Milliron, "The Interplay of Shape and Crystalline Anisotropies in Plasmonic Semiconductor Nanocrystals," *Nano Lett.*, vol. 16, no. 6, pp. 3879–3884, 2016, doi: 10.1021/acs.nanolett.6b01390.
- [39] K. Adachi, Y. Ota, H. Tanaka, M. Okada, N. Oshimura, and A. Tofuku, "Chromatic instabilities in cesium-doped tungsten bronze nanoparticles," *J. Appl. Phys.*, vol. 114, no. 19, 2013, doi: 10.1063/1.4831950.
- [40] K. Adachi and T. Asahi, "Activation of plasmons and polarons in solar control cesium tungsten bronze and reduced tungsten oxide nanoparticles," *J. Mater. Res.*, vol. 27, no. 6, pp. 965–970, 2012, doi: 10.1557/jmr.2012.25.
- [41] S. Heo, S. H. Cho, C. J. Dahlman, A. Agrawal, and D. J. Milliron, "Influence of crystalline and shape anisotropy on electrochromic modulation in doped semiconductor nanocrystals," *ACS Energy Lett.*, vol. 5, no. 8, pp. 2662–2670, 2020, doi: 10.1021/acsenerylett.0c01236.
- [42] H. Takeda and K. Adachi, "Near infrared absorption of tungsten oxide nanoparticle dispersions," *J. Am. Ceram. Soc.*, vol. 90, no. 12, pp. 4059–4061, 2007, doi: 10.1111/j.1551-2916.2007.02065.x.
- [43] R. D. Near, S. C. Hayden, R. E. Hunter, D. Thackston, and M. A. El-Sayed, "Rapid and efficient prediction of optical extinction coefficients for gold nanospheres and gold nanorods," *J. Phys. Chem. C*, vol. 117, no. 45, pp. 23950–23955, 2013, doi: 10.1021/jp4082596.

- [44] C. M. Staller, S. L. Gibbs, C. A. Saez Cabezas, and D. J. Milliron, "Quantitative Analysis of Extinction Coefficients of Tin-Doped Indium Oxide Nanocrystal Ensembles," *Nano Lett.*, vol. 19, no. 11, pp. 8149–8154, 2019, doi: 10.1021/acs.nanolett.9b03424.
- [45] S. V. Boriskina *et al.*, "Losses in plasmonics: from mitigating energy dissipation to embracing loss-enabled functionalities," *Adv. Opt. Photonics*, vol. 9, no. 4, p. 775, 2017, doi: 10.1364/aop.9.000775.
- [46] A. Hussain, R. Gruehn, and C. H. Rüscher, "Crystal growth of alkali metal tungsten bronzes M_xWO_3 ($M = K, Rb, Cs$), and their optical properties," *J. Alloys Compd.*, vol. 246, no. 1–2, pp. 51–61, 1997, doi: 10.1016/S0925-8388(96)02470-X.
- [47] B. Tandon, S. L. Gibbs, B. Z. Zydlewski, and D. J. Milliron, "Quantitative Analysis of Plasmonic Metal Oxide Nanocrystal Ensembles Reveals the Influence of Dopant Selection on Intrinsic Optoelectronic Properties," *Chem. Mater.*, vol. 33, no. 17, pp. 6955–6964, 2021, doi: 10.1021/acs.chemmater.1c01951.
- [48] P. Berini, "Plasmon-polariton waves guided by thin lossy metal films of finite width: Bound modes of symmetric structures," *Phys. Rev. B - Condens. Matter Mater. Phys.*, vol. 61, no. 15, pp. 10484–10503, 2000, doi: 10.1103/PhysRevB.61.10484.
- [49] X. Zeng *et al.*, "The preparation of a high performance near-infrared shielding Cs_xWO_3/SiO_2 composite resin coating and research on its optical stability under ultraviolet illumination," *J. Mater. Chem. C*, vol. 3, no. 31, pp. 8050–8060, 2015, doi: 10.1039/c5tc01411e.
- [50] T. Bronzes and S. Yellow, "The Electrical Conductivity of Sodium Tungsten Bronzes," *J. Am. Chem. Soc.*, vol. 71, no. 2, pp. 683–687, 1949.
- [51] P. Taylor, E. Salje, and B. Güttler, "Anderson transition and intermediate polaron formation in WO_{3-x} Transport properties and optical absorption," no. September 2011, pp. 37–41, 2006.
- [52] I. Oxyfluorides, "Tungsten and Molybdenum Oxyfluorides of the Type $MO_{3-x}F_x$," vol. II, no. 7, pp. 321–324, 1989.

TOC graphic

